

Full length article

Spatiotemporal slip dynamics during deformation of gold micro-crystals

G. Sparks^a, P. Sudharshan Phani^b, U. Hangen^c, R. Maaß^{a,*}^a Department of Materials Science and Engineering, University of Illinois at Urbana-Champaign, Urbana, IL 61801, USA^b Nanomechanics Inc., 105 Meco Ln, Oak Ridge, TN 37830, USA^c Hysitron, Inc., Dennewartstrasse 25, 52068 Aachen, Germany

ARTICLE INFO

Article history:

Received 22 April 2016

Received in revised form

1 September 2016

Accepted 15 September 2016

Keywords:

Dislocation avalanches

Plasticity

Intermittency

Micro-compression

ABSTRACT

Intermittent plastic deformation in micro-crystals was resolved in both space and time, yielding velocity profiles that peak in a range from approximately 1 $\mu\text{m/s}$ to 100 $\mu\text{m/s}$. The peak velocities exhibit a broad, close to scale-free distribution, with a scaling regime at high velocities that is compatible with a cubic decay. Slow slip dynamics in the $\mu\text{m/s}$ regime show an approximately flat distribution. An apparent power-law scaling between peak slip-velocity and event size was also observed. The spatiotemporal dynamics of the dislocation-mediated plastic intermittency is discussed in terms of lateral and vertical slip-step growth velocities, where the vertical growth velocity is ~ 4 orders of magnitude slower than the lateral dislocation-group velocity, providing a rationale for the measured slow dynamics. In order to validate the experimental results, the response of the used nanoindenter is evaluated for the time during the plastic instability. Fracture tests on Si were conducted to determine the upper bound in dynamic response of the device. Finally, in-situ electrical contact measurements complete the suite of tests that unequivocally demonstrate that the used nanoindentation platform is capable of tracing the spatiotemporal slip dynamics during slip of small-scale crystals.

© 2016 Acta Materialia Inc. Published by Elsevier Ltd. All rights reserved.

1. Introduction

Plastic deformation of crystals is mediated via the movement of dislocations. During application of an increasing stress, the underlying dislocation structure is known to respond intermittently, where the majority of the dislocation network remains immobile but a certain group of dislocations quickly rearranges to relax local stresses. These sudden rearrangements can be recorded as an acoustic emission pulse [1], or directly as discrete stress-strain data from ultra-high-resolution mechanical experiments on macroscopic samples [2,3]. Recent progress in nano- and micro-mechanical testing reinvigorated interest in this intermittent plastic flow because the stress-strain curves of nano- or micron-sized single-crystals exhibit a vast number of sudden strain bursts, which are associated with these moving groups of dislocations, also called dislocation avalanches [4]. Commonly, the micro-compression technique using a nanoindenter platform is employed to record intermittent stress-strain data (see Fig. 1) that can be

analyzed with respect to the slip-size statistics. It has been shown that the event size probability distributions obtained from deforming micro- and nano-crystals exhibit some degree of scale-free power-law behavior with the scaling exponents typically around 1.5 [5–10], and recent discussions focus on the factors influencing the value of this scaling exponent [11–14]. In general, the experimental findings are well in agreement with theoretical predications [15] and dislocation dynamics (DD) modeling [16–18].

In our recent work, we explored the micro-compression method further, using data sampling rates of several kHz in order to probe the slip dynamics; that is, the transient phase between the onset and end of the slip event [19,20]. This allowed the assessment of the apparent slip-velocities during slip events in addition to the usual slip-size data. The obtained slip-size magnitudes displayed the expected probability distribution representing scale-free scaling, and furthermore the obtained slip-velocities showed a probability distribution scaling compatible with the predictions of 3D dislocation dynamics (DD) simulations [21] and theoretical analysis of avalanches near the depinning transition [18]. In addition to these results reflecting known properties of dislocation-mediated plasticity, no apparent scaling between crystallographic slip-velocity

* Corresponding author.

E-mail address: rmaass@illinois.edu (R. Maaß).

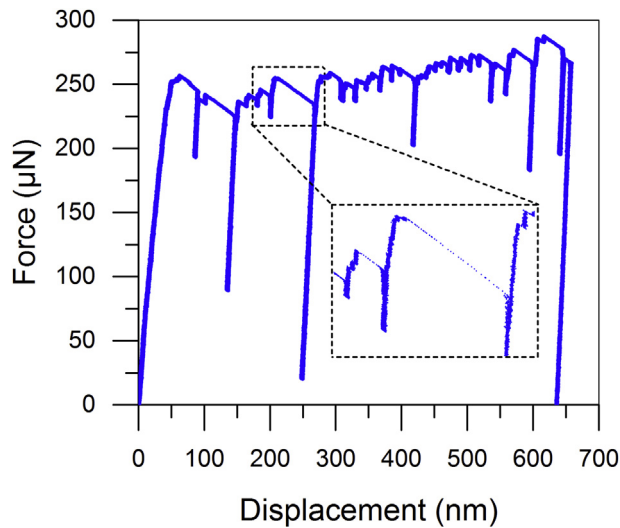


Fig. 1. Representative load versus displacement curve for micro-column compression testing. The zoomed inset shows the behavior of the load-displacement curve during strain bursts. Substantial elastic unloading after a strain burst is due to the controller reducing the applied force to counteract the sudden increase in displacement beyond the specified displacement rate in displacement control.

and applied stress could be established across a range of more than 400 MPa [19]. This was rationalized on the basis of microplasticity in which fluctuations of an internal stress field form a static component, and dynamic interactions with other dislocations dominated the dynamic response of the avalanche. In view of the classical result of a strongly stress dependent dislocation velocity [22–24], v_d , empirically known as $v_d = v_0(\tau/\tau_0)^m$, with the materials parameters v_d , τ_0 and $m \gg 1$, it is expected that the dislocation velocity at the size-affected stresses will be very high. Given that a slip event (dislocation avalanche) is mediated by dislocation movement, it could be expected that the slip-velocity should also be very fast, and questions arise as to what extent the data truly represents a dislocation-mediated process. This is indeed a valid question, which urges for additional investigations on the validity of slip-kinetics measurements done with a nanoindenter (here a Hysitron TriboIndenter). In fact, if indeed the measured slip-kinetics are entirely unrelated to the underlying plasticity, then it is not clear why the distribution of slip-sizes or slip-velocities scale as expected from theoretical predications and as shown in DD-modeling of intermittent plasticity.

The main problem lies in the unclear link between the measured slip-velocity and the underlying dislocation velocity [20]. Clearly, the slip event (dislocation avalanche) represents a collective motion, where the slip-size magnitude can be understood as the lower bound of the net Burgers vector content of the instability. Taking a typical slip-size of 2 nm in a 2 μm sized crystal, and the Burgers vector for Au, this results in at least 10 dislocations that are deposited onto the surface during slip. The flow stress level of such a micro-crystal is ca. 95 MPa [20]. Using the classical picture of linearly stress dependent dislocation velocities for the high-stress/high-velocity regime, $v_d = \frac{b\tau}{B}$ (where B is a material constant representing viscous drag on the dislocation) [25] gives $v_d > 100$ m/s for $\tau = 95$ MPa, which leads to the conclusion that the approximate slip-duration for the consecutive motion of 10 dislocations (constantly emitting source) would be ca. 200 ns or less. This is clearly incompatible with earlier results that showed that slip-durations are of the order of some hundred μs to several ms when sampled at 7 kHz [19,20]. With this large discrepancy between the expected underlying dislocation velocity and the measured slip-

velocity (when large enough sampling rates are used), one would need to conclude that during the majority of the measured slip-duration no actual dislocation activity is taking place, but that the slipping crystal primarily is at rest or in a quiescent avalanche state. The simple estimate above would yield an inactive phase of about $1 - (200 \text{ ns})/(2 \text{ ms}) = 99.99\%$; an inconsistency that was already articulated during the 1960s, when velocities of individual or grouped dislocations were measured [26]. Either the slip event is indeed fast, but broken up in a series of alternating active or inactive stages that are beyond the experimental resolution, or the number of dislocations is substantially underestimated, or finally it may be that the device is not able to trace the slip event properly. In the latter case, the indentation tip would be expected to lose contact with the slipping crystal, which would need to continue its dynamic phase without any applied stress, and one would have to question whether the slip-sizes derived from such measurements are reliable. Elastic relaxation of the column could allow for contact to be maintained even if the tip cannot move at sufficient speed to follow the plastic deformation of the column, but given the observed applied forces and pillar stiffness, the elastic relaxation (length increase) can be at most ~ 13 nm, which is insufficient to maintain contact for the larger event sizes. Thus, the situation is unsatisfactory, and the aim of the following work is to shed further light onto the underlying collective dislocation dynamics during a slip event measured in a small-scale deformation experiment with a nanoindenter, and also to support the view that it can be excluded that the device is losing contact with the slipping crystal.

We will first follow the approach of Hay et al. [27] that modeled the nanoindenter as an underdamped linear harmonic oscillator, which allows us to estimate the indenter dynamics. The modeled dynamics of the device can then be compared to the measured values during slip events, the results of which imply that the force from the sample on the indenter tip does not fall to zero at any point during the slip events. Secondly, the peak velocities of the indenter tip measured during events in various materials are discussed and compared with those from a known loss-of-contact scenario that was evaluated by tracing the indenter response after fast fracture of silicon micro-samples. Thirdly, in-situ electrical contact measurements are done on micron sized crystals, with the aim at exploring if a loss of current can be recorded during the slip phase. The summarized findings of these efforts clearly indicate that contact is not lost between the slipping crystal and the nanoindenter.

Following this, further analysis is done on the characteristics of the slip events themselves. The force-displacement behavior of the sample during slip events is compared to that during elastic loading and unloading, demonstrating that the effective sample stiffness during slip events is lower than the axial quasi-static stiffness, and thus suggesting that the samples are indeed plastically deforming during the displacement jump representing the slip event.

Inspection of the velocity profiles in some events suggests that they may be multiple temporally overlapping slip events, and an algorithm designed to separate or discard such events results in the elimination of the two-branch structure seen in earlier work by removing all of the “slow” events [19,20]. This carries the implication that such events may simply be multiple slip events that could not be well separated during initial data extraction and analysis. Inspection of the peak velocities during slip events in FCC Au shows a power-law correlation with event size, which is compared with that found for BCC Mo [5] and theoretical values from mean-field theory [18]. Finally, we propose that the large discrepancy between collective dislocation velocities and the here measured slip-velocities finds its origin in the large ratio between laterally and vertically growing slip-steps – a view compatible with classical findings on slip-line cinematography [22].

Table 1
Sample and test details.

| Sample material | Nominal sample size (μm) | Test type | Machine used | Control mode | Strain rate/force rate | Data acquisition rate (kHz) |
|--------------------|---------------------------------------|--------------------|--------------|-------------------------|------------------------|-----------------------------|
| Au | 2 | Column compression | TI-950 | Displacement control | 1×10^{-2} | 16 |
| Ni ₃ Al | 1.5 | Column compression | TI-950 | Displacement control | 1×10^{-2} | 16 |
| Vit105 | 1 | Column compression | TI-950 | Displacement control | 1×10^{-2} | 16 |
| Si | 1 | Column compression | TI-950 | Displacement control | 1×10^{-2} | 16 |
| Au | 2 | Column compression | NanoFlip | Open-loop force control | 50 $\mu\text{N/s}$ | 100 (disp. only) |
| Au | 2 | NanoECR | TI-950 | Displacement control | 3.5×10^{-3} | 7 |
| Au | 2 | NanoECR | TI-950 | Open-loop force control | 30 $\mu\text{N/s}$ | 7 |
| Si | $2 \times 2 \times 12$ | Beam bending | TI-950 | Open-loop force control | 60 $\mu\text{N/s}$ | 16 |

2. Experimental details

Micro-compression experiments were conducted on single-crystal Au columns. The samples had an [001]-compression axis and were cut from a bulk single-crystal by means of annular milling with a focused ion beam. Other columns were similarly produced from bulk single-crystal Si, bulk single-crystal Ni₃Al, and Vit105 bulk metallic glass (Zr_{65.7}Cu_{15.6}Ni_{11.7}Al_{3.7}Ti_{3.3}). Micro-compression testing was done in a Hysitron TriboIndenter TI-950 with a nanoDMA[®] III transducer and performech[™] control unit, with a raw data acquisition rate of 78 kHz averaged across multiple samples to the desired effective rate on all channels. Several gold samples were also tested by Nanomechanics Inc. (NMI) using their commercially available NanoFlip platform (with a data acquisition rate of 100 kHz on the displacement channel only) in order to compare the peak velocities obtained with the two machines. The data from the NMI samples was not used for analysis other than what is presented in Section 3.2.

In addition to regular compression experiments, in-situ electrical contact resistance measurements (ECR) were performed with the Hysitron nanoECR[®] module [28,29]. During these in-situ tests, a constant voltage was applied during the deformation experiment. In that way, the evolution of the current could be recorded during intermittent plastic flow. A conductive boron diamond tip was used as a compression tool. The samples used for the ECR tests were single-crystal Au columns identical to the ones described above. Prior to testing with the nanoECR[®] module, the flat end of the tip was iteratively cleaned and imaged to ensure a high quality electrical contact. The data from these samples was not used for analysis other than what is presented in Section 3.3.

Several Si cantilevered beams were also fabricated for indenter fracture response testing, as after fracture of a Si column the indenter tip would rapidly accelerate downwards and strike the bulk substrate of the sample, preventing the indentation tip from oscillating freely. These beams were tested in bending, with the indenter tip pressing down on the end of the beam.

Table 1 below contains details on the samples and test conditions for each test presented in this paper. The given column sample size is the diameter, and the columns have a nominal aspect ratio (height/diameter) of ~3.

3. Results

3.1. Modeling the indenter dynamics

Understanding the dynamic response of a nanoindenter is not a trivial task, particularly if one considers the control feedback that interferes with the mechanical response of the tip suspended by a spring on one end, and in contact with the sample on the other end. From a purely mechanical approach, Hay and co-workers [27] have successfully shown that a simplified nanoindenter can be described with the following equation of motion:

$$m\ddot{z}(t) + D\dot{z}(t) + Kz(t) = 0 \quad (1)$$

where $z(t)$ is the time-dependent position of the mass m attached in parallel to a spring with stiffness K and a dashpot with viscous damping D (i.e., the system is modeled as a damped harmonic oscillator). This simplification reduces the sample stiffness, spring stiffness and frame stiffness of the experiment to one effective spring with stiffness K , and the effective damping of both the indenter and the tested material are combined in D . Solving this differential equation yields a solution that is of the known form for an underdamped linear harmonic oscillator,

$$z(t) = \exp(-\delta_i t) (\delta_i z_0 / \omega_d \times \sin(\omega_d t) + z_0 \cos(\omega_d t)) \quad (2)$$

with the indenter damping coefficient $\delta_i = D/2m$, the initial deflection away from equilibrium z_0 , and the resonance frequency $\omega_d = \sqrt{(\omega_0^2 - \delta_i^2)}$, where ω_0 is the natural frequency of the transducer: $\omega_0 = \sqrt{K/m}$.

The damping coefficient and resonance frequency of the transducer were not initially known, so the analytic solution given in Equation (2) could not be used directly. In order to determine the oscillation characteristics of the indenter, fracture of one of the silicon cantilevered beam samples in open-loop force-control mode was used to provide an effective impulse force input (i.e. the net force on the indenter tip increased very rapidly), and a damped sinewave equation was fit to the resulting oscillation. This fit is shown in Fig. 2, with the fitting equation being of the simplified form

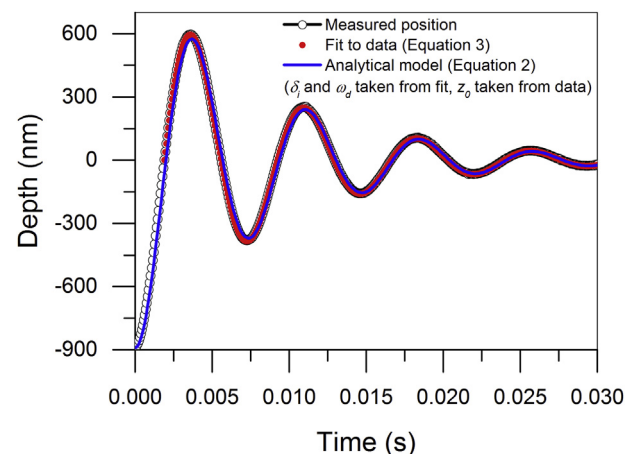


Fig. 2. Displacement as a function of time recorded in open-loop control mode after fracture of a Si cantilevered beam. The data has been fit to Equation (3), a damped sinewave, and is compared with Equation (2), which is the analytical solution for a damped harmonic oscillator released from rest at nonzero z .

$$A \exp(-\delta_i(t - t_0)) \sin(\omega_d(t - t_0)) \quad (3)$$

with $A = 730$ nm, $\delta_i = 118$ s⁻¹, and $\omega_d = 854$ s⁻¹ determined from the fit. The position data in Fig. 2 was shifted from the raw data to put the final equilibrium depth at 0 nm and the time of initial fracture at 0 s. For Equation (3), t_0 was taken as the time of the first zero crossing of the shifted depth data. Depth values calculated using the analytical solution given in Equation (2) are also included in the plot for comparison, showing excellent agreement with the measured data.

The elastic stiffness K of the transducer was found to be 319 N/m by fitting the force/displacement behavior during strain burst events in open-loop control mode [30]. This allowed the calculation of the indenter system sprung mass $m = K/\omega_0^2 = 0.429$ g and damping coefficient $D = 2m\delta_i = 0.101$ N-s/m. The values obtained using this fitting method can be compared with the values subsequently obtained via dynamic mechanical analysis (DMA) self-calibration of the transducer, which were $K = 361$ N/m, $m = 0.445$ g, and $D = 0.0904$ N-s/m. The observed good agreement is encouraging for application of this technique to transducers that do not necessarily have DMA capability.

Taking the measured force $F(t)$ and position $z(t)$ from the indenter, as well as the spring, mass, and damping constants that were determined above, and using finite difference derivative approximations to find the velocity $v(t)$ and acceleration $a(t)$ from $z(t)$,

$$v(t) = (z(t + \Delta t) - z(t - \Delta t)) / (2\Delta t) \quad (4)$$

$$a(t) = (z(t + \Delta t) - 2z(t) + z(t - \Delta t)) / \Delta t^2 \quad (5)$$

we can solve $\sum F = ma$ for the approximate external force $F_{ext}(t)$ on the indenter tip necessary to produce the observed displacement behavior. The final equation is then

$$F_{ext}(t) = F(t) - ma(t) - Dv(t) \quad (6)$$

Note that the spring constant K does not appear in Equation (6), as the transducer calibration ensures that the measured force $F(t)$ already includes the force applied by the transducer springs. The finite difference calculations are done after smoothing the displacement data with a low-pass filter, as otherwise the finite difference equations amplify the noise to an excessive degree. Care must be taken when selecting the filter details; too little filtering will result in overwhelming noise, while excessive filtering helps eliminate noise but may suppress fine details and extend the event duration. The filter used was a 30th-order finite impulse response filter, applied to each event individually with a cutoff frequency of $f_c = 1/dt$ (where dt is the event duration) created using Matlab's `fir1` command.

Figure 3a gives an example of the external force calculation for fracture of one of the silicon cantilevered beam samples. Note that $F_{ext}(t)$ initially matches $F(t)$ very well (i.e. acceleration and velocity are both near-zero and the indenter tip is in quasi-static equilibrium with the sample), but at the beginning of the fracture event $F_{ext}(t)$ drops approximately to zero very rapidly and remains there for the rest of the test, as would be expected for the reaction force from a sample fracturing and losing contact with the indenter tip. This differs from the measured force $F(t)$, which remains nonzero throughout the event. This supports the assumption (used in this paper) that $F_{ext}(t)$ can be used to represent the contact reaction force from the sample (and thus the force applied to the sample), which does not necessarily match the measured force value $F(t)$ from the machine during non-quasi-static events.

Examining the behavior of $F_{ext}(t)$ during slip events from Au

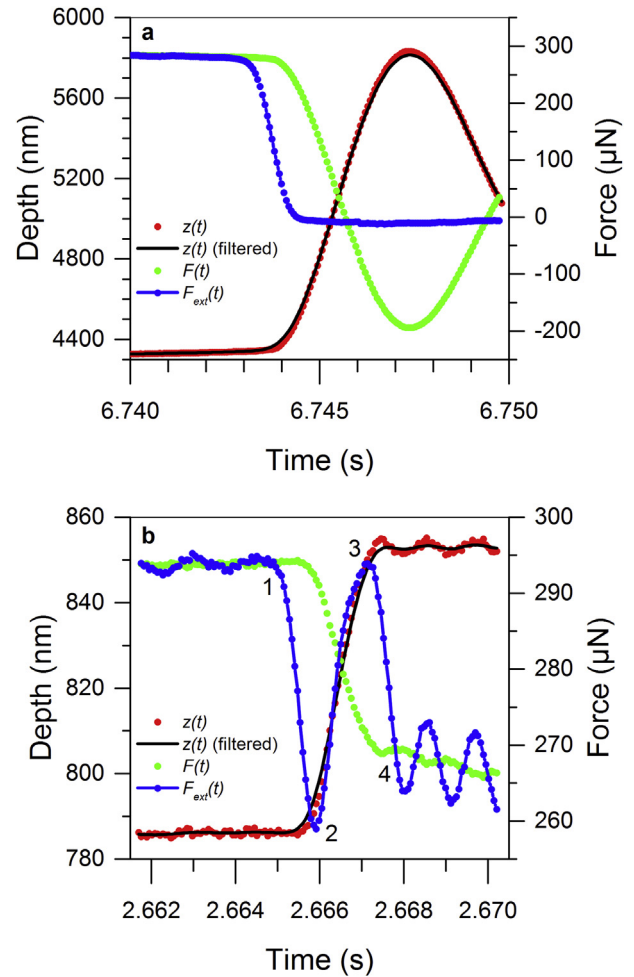


Fig. 3. a) Fracture event of a Si cantilevered beam with comparison of $F_{ext}(t)$ and $F(t)$. Note that $F_{ext}(t)$ drops to near-zero very quickly, while $F(t)$ remains nonzero throughout the dynamic motion. $z(t)$ is the raw position signal, which can be compared to the smoothed data, labeled “ $z(t)$ (filtered)”. b) Au column slip event with comparison of $F_{ext}(t)$ and $F(t)$. Numbered points 1–4 label specific portions of $F_{ext}(t)$, with the behavior in each section discussed in the text.

columns (shown in Fig. 3b) proves instructive. While it initially drops noticeably during an event, it never drops to zero. For all samples tested that exhibited slip events (Au, Ni₃Al, and Vit105), the largest drop in $F_{ext}(t)$ is only a small fraction of the applied force, with the values given below in Table 2. This contrasts with the fracturing Si pillars or beams, which show the force drop being ~100% of the applied force at the time. The slightly negative reaction force calculated for the Si samples is most likely due to residual noise after filtering.

Since the values of the force drops for the metals are much smaller than for the fracturing Si samples both as a percentage of the applied force and in absolute terms, it is clear that the indenter tip does not lose contact with the sample during slip events. Figure 3b plots a large slip event with the largest drop in $F_{ext}(t)$ for the gold samples. This consists of a rapid drop to some value below the applied force (between points 1 and 2 in Fig. 3b), a period of increase at a roughly constant rate to a value above the applied force (between points 2 and 3), another rapid drop down to the applied force (between points 3 and 4), and finally a period of more minor elastic oscillations around equilibrium with the applied force (after point 4). This last occurs while the feedback control reduces the applied force on the indenter tip, in order to return the

Table 2

Details of the largest differences between the directly measured electrostatic force applied to the indenter tip by the transducer and the calculated reaction force from the samples.

| Material | Electrostatic force (μN) | Reaction force (μN) | Absolute difference (μN) | Difference (%) |
|--------------------|---------------------------------------|----------------------------------|---------------------------------------|----------------|
| Au | 292 | 258 | 34 | –11.6% |
| Ni ₃ Al | 2491 | 1967 | 524 | –21.0% |
| Vit105 | 1589 | 1459 | 130 | –8.28% |
| Si pillar | 3741 | –64 | 3805 | –101.7% |
| Si beam | 266 | –30 | 293 | –110.1% |

displacement to the lower value specified by the load function. The oscillation is a known consequence of the feedback control reacting to a rapid change in the controlled variable (in this case the displacement), and can also be observed in the measured depth values.

3.2. Peak velocities in gold, silicon, nickel-aluminide, and metallic glass

One might expect that, if the nanoindenter had a maximum velocity that could be achieved by the indentation tip, that this would be reflected as a consistently observed maximum velocity across a variety of samples. A range of column materials were tested in order to determine if such a maximum velocity is observed, with the results shown in Fig. 4. The range of observed peak velocities is very wide (an order of magnitude or more) even within a single material; such a wide range of events is an indication of scale-free intermittent plasticity [6,20]. The observed mean velocities and standard deviations were as follows: $v = 6.0 \mu\text{m/s}$ and $\sigma = 5.4 \mu\text{m/s}$ for Au, $v = 6.3 \mu\text{m/s}$ and $\sigma = 4.3 \mu\text{m/s}$ for NMI Au (Au columns tested by Nanomechanics Inc., see Section 2 and Table 1), $v = 32 \mu\text{m/s}$ and $\sigma = 62 \mu\text{m/s}$ for Ni₃Al, $v = 54 \mu\text{m/s}$ and $\sigma = 57 \mu\text{m/s}$ for Vit105, and $v = 1.7 \text{ mm/s}$ and $\sigma = 1.8 \text{ mm/s}$ for Si.

The Au data-set in Fig. 4 had the largest number of tested samples and thus the most observed events (ca. 1400). As can be seen in Fig. 4, the substantially higher sampling rate of the NMI-device (see Section 2 and Table 1) does not significantly alter either the mean or the individual velocity of the slip events measured. The smaller standard deviation of the data obtained with the NanoMechanics device is ascribed to the smaller number (ca. 120) of events available.

Data from events in Ni₃Al columns are also shown, demonstrating much higher peak event velocities ($\sim 8\times$ larger on average

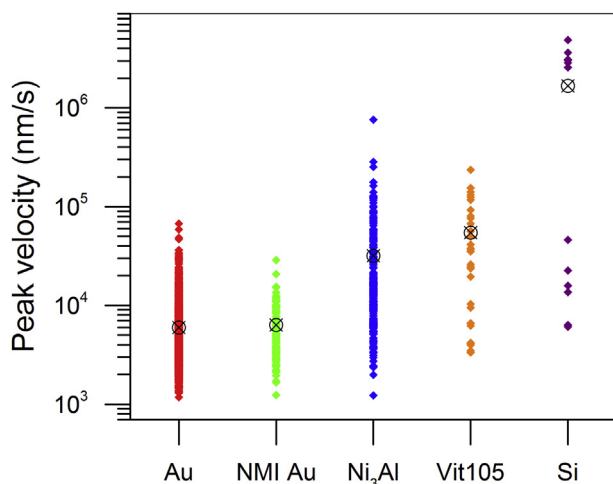


Fig. 4. Scatter bar chart of peak event velocities for Au columns tested with a Hysitron nanoindenter and with a NanoMechanics Inc. (NMI) nanoindenter, Ni₃Al columns, Vit105 metallic glass columns, and Si columns. The mean value of the peak velocities for events in a given material is also indicated on the chart by the crossed circles.

than for the Au samples). This is partially due to the typically greater size of slip events in the Ni₃Al samples relative to the gold samples ($\sim 26 \text{ nm}$ vs $\sim 6 \text{ nm}$ on average), as it is known that the event size correlates with the peak event velocity in such experiments [5]. This is not taken into account in Fig. 4, but when comparing events of similar size there is still a discrepancy, with the Ni₃Al events remaining faster by approximately a factor of 2.

Furthermore, Fig. 4 includes slip-velocity data from a Vit105 metallic glass. The shear velocity for this metallic glasses has been investigated in depth at the bulk scale [31,32]. There, the typical event velocity was found to be on the order of $500 \mu\text{m/s}$ when resolved along the shear band planes at 45° to the compression axis, or $350 \mu\text{m/s}$ along the compression axis. Here the mean peak axial velocity is found to be $53 \mu\text{m/s}$, nearly an order of magnitude smaller, although the fastest event reaches $230 \mu\text{m/s}$. This lowered velocity in small-scale metallic glass compression experiments is consistent with results from analytical modeling [33] and *in-situ* TEM nano-compression testing [34]. Despite the lowered velocity relative to macroscopic bulk metallic glass samples, the mean value is still an order of magnitude larger than that for the gold samples.

For the data from the silicon columns, the highest event velocities do not represent crystallographic slip, but rather fast fracture of the entire column followed by rapid forward movement of the indenter tip. In these tests, the tip has lost contact with the sample. The obtained forward surge velocities are at least an order of magnitude higher than those obtained for any of the other samples, reaching several mm/s . As these velocities can reasonably be taken as the upper limit for the velocity of the indenter tip, the fact that they are greater than for the other samples provides evidence that the indenter tip can indeed move with sufficient velocity to remain in contact with the metallic samples. The several lower velocities (below 10^5 nm/s) seen in the silicon data in Fig. 4 are due to partial crack propagation events, resulting in only a slight shift in the position of the column tip and occurring prior to complete fracture of the column.

The extremely high velocities reached for the silicon fracture events are attributed to the loss of contact with the sample while the transducer is applying a substantial force (up to several mN) to the indenter tip. Prior to fracture, this force was in equilibrium with the contact reaction from the sample, but after fracture it is unopposed, which causes the indenter tip to begin accelerating downwards at a very high rate (on the order of 10 m/s^2). Even for smaller applied forces $F(t)$, the maximum achievable acceleration without requiring that F_{ext} drops to zero (i.e., without losing contact with the sample) remains high, e.g. $\sim 0.25 \text{ m/s}^2$ for a force difference of only $100 \mu\text{N}$. The very low mobile mass of the transducer/tip system is critical for allowing this capacity for rapid acceleration.

3.3. In-situ nano-electrical contact resistance measurements

For additional confirmation that contact is maintained with the sample during slip events, we turn to *in-situ* nano-electrical contact resistance measurement (ECR). This technique applies a voltage to a conductive indenter tip and measures the current flowing through the tip and into the sample during an indentation test. If contact

were lost, the continuous flow of current through the tip and into the sample should be interrupted, which would be observable in the current measurement data. A DAR of 7 kHz was used for all data in these tests.

Figure 5a shows a typical force-displacement curve obtained from the ECR tests with an applied voltage of 3 mV in displacement control (DC) mode. After an initial apparent elastic response, plastic flow sets in at about 300 μN (~90–100 MPa).

In addition to the force-displacement data, the current I is displayed in Fig. 5a. It can be seen, particularly at low displacements, that each time there is displacement jump a small drop in the current signal appears. This coincides with the device-controlled elastic unloading after each event. There is thus a clear correlation with applied force and current level that can be monitored during deformation, possibly related to changes in contact area and/or contact resistance caused by the changing force. Changes in current can also be caused by microstructural changes (e.g. a sudden change in dislocation density) that alter the overall resistivity of the sample.

More insightful for the in-situ electrical contact study is to investigate the evolution of the current throughout one of the displacement jumps. Since it was shown earlier that larger events are faster for both FCC [19,20] and BCC [5] crystals (which is in agreement with crystal plasticity modeling [35,36]), a close-up of the data for a large displacement jump of 25 nm is displayed in Fig. 5b. This plot shows no indication of any current drop during the forward surge of the indentation tip, which implies that within the time resolution (ca. 0.1 ms) of the measurements the slipping crystal remains in contact with the compression tip. Figure 5d shows a plot of force versus current before and after this slip event,

confirming that while the absolute value of the current at a given force changes after the deformation of the sample, the slope of the force-current relationship remains very similar, and would therefore presumably reveal any significant force drops. We also observe continuous current for the other steering modes, which are closed-loop force-controlled and open-loop force-controlled deformation. Figure 5c shows a similar plot to Fig. 5a for data obtained using open-loop force-controlled deformation. While the current does decrease during the early large event, it does not fall to zero. A drop in current is also consistent with the drop in measured force during the event.

4. Discussion

4.1. Sample-tip contact during slip events

The evidence presented here points towards contact being maintained between the indenter tip and the sample during slip events. In Section 3.1, it was demonstrated that the calculated reaction force falls to zero during known loss-of-contact events, but does not do so during any of the observed slip events in Au, Ni₃Al, or Vit105 metallic glass samples. In Section 3.2, different materials showed dramatically different maximum velocities, with fracture-based loss-of-contact events of Si samples having the highest velocity, exceeding the velocities obtained from the metallic samples by 1–1.5 orders of magnitude. If the indenter system was the limiting factor on velocity, we would expect to observe a cap on the velocity, with all materials showing event velocities at or below this cap, which is not seen. The silicon fracture events in displacement control might reasonably be considered as such a limit, as the

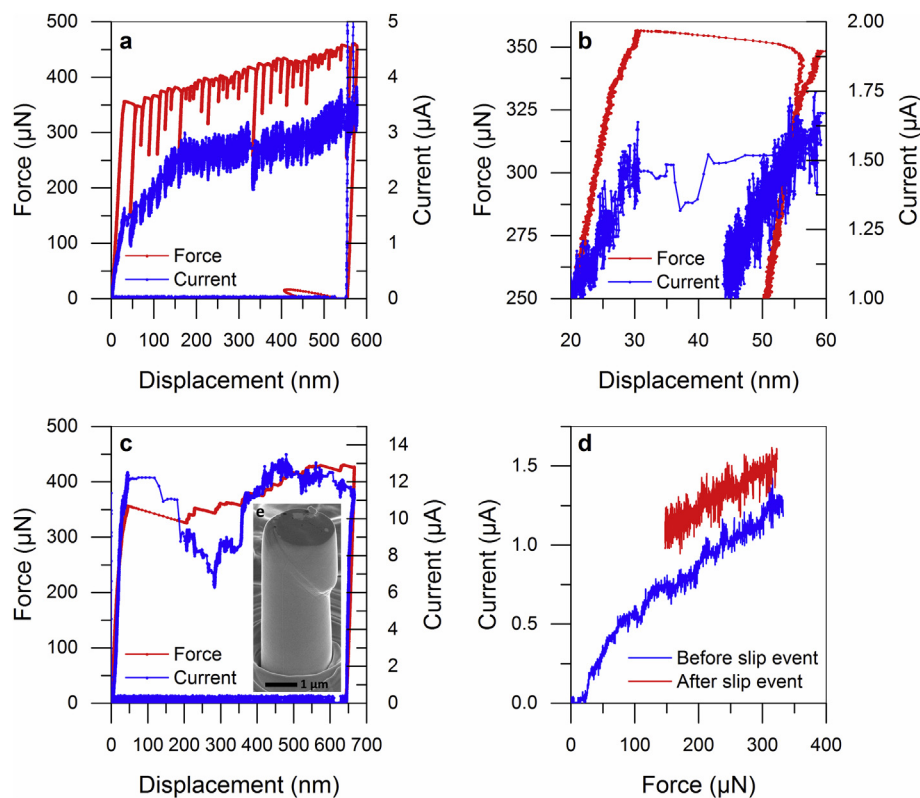


Fig. 5. a) Force-displacement and current-displacement data recorded during in-situ electrical contact measurement of an Au column in displacement controlled (DC) steering mode. b) A close-up view of the first large displacement jump of the data shown in a). c) Force-displacement and current-displacement data recorded during in-situ electrical contact measurement of an Au column in force-controlled open-loop steering mode. d) A plot of force versus current during elastic deformation before and after the slip event shown in b). e) SEM image of column after nanoECR testing. The applied voltage was 3 mV for all of the tests. See Table 1 for other test details.

combination of fast fracture and displacement control mode results in the indenter tip being driven forward by a substantial and unopposed applied force, which produces the maximum possible acceleration for the indenter tip. Given that this maximum velocity is far higher than that observed for any of the sample types, it can be concluded that the limiting factor is the sample and not the testing machine, such that the machine can remain in contact throughout the event. Finally, in Section 3.3, the ECR measurements show that current is maintained throughout slip events, with the implication that contact is maintained as well. In the light of the clear correlation between the ECR current and the quasi-static applied force on the sample (observed in Fig. 5d), the lack of substantial current drop during events in displacement control also supports the conclusion in Section 3.1 that the force on the sample does not drop substantially during slip events. The possibility remains that the current could still flow while mechanical contact is lost. However, in such a situation an arc must form, which should be directly seen in the current signal as well as leave traces on the crystal surface. To exclude this possibility, and to strengthen our conclusion, a scanning electron micrograph of an ECR deformed specimen is shown as an inset in Fig. 5e. The deformation morphology is identical to those known from regular micro-compression testing and does not show any evidence of arcing.

4.2. Plastic response during slip events from $F_{ext}(t)$

The behavior of the calculated force on the sample, $F_{ext}(t)$ (see Section 3.1), displays substantial differences from that of the measured force value $F(t)$ taken directly from the transducer during non-quasi-static situations, i.e. slip events. During the majority of an event, $F_{ext}(t)$ typically increases at a fairly constant rate relative to the displacement, with the typical behavior shown in Fig. 6a. This is contrasted with the measured $F(t)$, which decreases linearly with increasing depth during the event, with the slope depending primarily on the stiffness of the transducer [30]. The average slope of the increasing portion of $F_{ext}(t)$ can be crudely approximated by a linear fit to the region between the local minimum (point 1 in Fig. 6a, corresponding to point 2 in Fig. 3b) and the local maximum (point 2 in Fig. 6a, corresponding to point 3 in Fig. 3b), giving an effective stiffness value during the dynamic portion of the slip event. When compared with stiffness values taken from linear fits during the elastic unloading and reloading after large slip events (e.g. Fig. 1 at approximately 250 nm), it is observed that the effective stiffness during slip events is always lower, as can be seen in Fig. 6b. The lowered stiffness relative to elastic deformation implies

that plastic deformation is indeed occurring during the whole of the slip event, as opposed to the possibility of a collective dislocation rearrangement occurring almost instantaneously within the sample. In such a case, the measured “slip event” would be the machine’s movement to a new point of elastic equilibrium after the rapid plastic rearrangement, and one would expect the measured “deformation” to reflect the elastic stiffness of the material.

The mean effective stiffness during the slip events is $3.28 \mu\text{N}/\text{nm}$ with a standard deviation of $1.81 \mu\text{N}/\text{nm}$. Given that this is substantially lower than even the lowest measured stiffness during quasi-static elastic loading ($10.3 \mu\text{N}/\text{nm}$), this clearly demonstrates the reduction in stiffness during the slip events. Using the nominal sample dimensions of $2 \mu\text{m}$ diameter and $6 \mu\text{m}$ height to convert force to engineering stress and displacement to engineering strain, the elastic stiffness value at low strain of $10.3 \mu\text{N}/\text{nm}$ gives a Young’s modulus of 19.7 GPa . This is within a factor of ~ 2 of the literature value of 43 GPa for $[001]$ -oriented single-crystal gold [37], which is a typical level of error for modulus measurements from micro-compression testing [38]. The slight increasing trend in the elastic stiffness with strain is due to the changing shape of the column as it plastically deforms, becoming shorter and wider and therefore stiffer (“geometric stiffening”), while there is no apparent trend in the data for effective stiffness during the events. Thus, we believe that plastic deformation is indeed occurring throughout the recorded slip events.

4.3. Slip event analysis – velocity profiles and event separation

Earlier work noted that plotting event size versus velocity produces a plot with two visible branches. The two branches were defined as “fast” events, having variable (and relatively large) sizes and short durations, and “slow” events, having low sizes and variable (and relatively long) durations [19,20]. Events with both very large sizes and very long durations were not seen. The cause of this observation was not initially clear, with the possibility of it being related to a microstructural mechanism resulting in bimodal dynamic behavior.

This behavior is investigated here with new data and analysis methods, with the reproduced two-branch behavior shown in Fig. 7a. Slip events in gold columns were extracted from raw data and analyzed using a semi-automated routine, as in the previous work [19]. A displacement and velocity profile of a “fast” event is shown in Fig. 7b, demonstrating the typical peaked velocity profile. For comparison, Fig. 7d shows a profile for an event with an unusually long duration for its size. The multiple peaks in the velocity

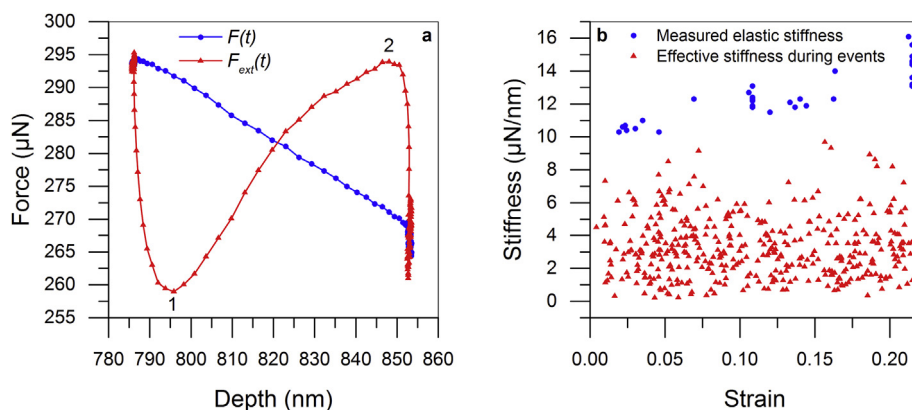


Fig. 6. a) $F(t)$ and $F_{ext}(t)$ versus depth during a slip event in an Au column. Points 1 and 2 are the local minimum and maximum, respectively. b) Elastic stiffness measured during unloading and reloading following large slip events in Au columns, and effective stiffness measured during slip events in said columns, both plotted versus strain at the time of the given measurement.

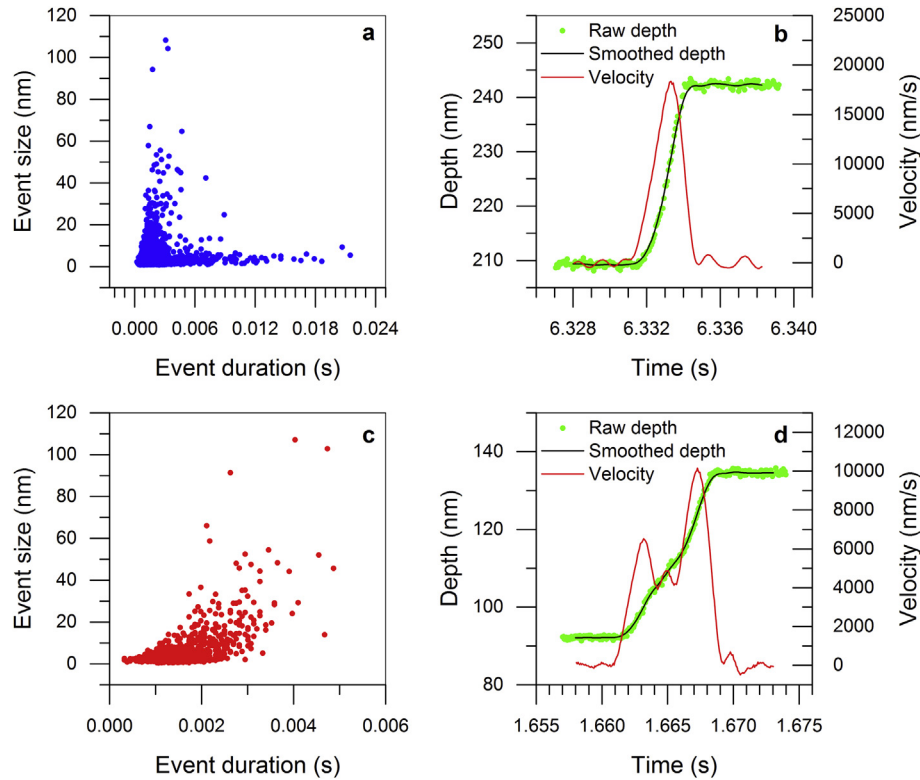


Fig. 7. a) Scatter plot of slip event size vs duration showing two-branch behavior. b) Depth and velocity profile of a “fast” slip event. c) Scatter plot of slip event size vs duration after an algorithm removed events with multiple velocity peaks. d) Depth and velocity profile of an event with an unusually long duration for its size, which would have been removed by the algorithm due to having multiple velocity peaks. All data is from Au columns.

profile of Fig. 7d suggest the possibility that the apparently single event may actually be multiple temporally overlapping slip events. If true, this would imply that some of the “slow” events could possibly be broken up into individual “fast” events. It is noted that the sampling rate used in this study is more than twice as high as the 7 kHz acquisition rate used in Refs. [19,20]. It therefore appears that 7 kHz is not fully sufficient to allow clear separation between events of the types shown in Fig. 7b and d.

An algorithm was developed to recalculate event boundaries and eliminate any events showing multiple velocity peaks. Interestingly, as shown in Fig. 7c, if the size-duration data is replotted after applying this algorithm, the “slow” event branch is entirely absent. This suggests that the previously observed long-duration events [19,20] may be due to multiple closely-spaced events of small size that earlier could not be easily distinguished from each other during event extraction. Note that this method cannot fully exclude the possibility that the cleaned events contain multiple sub-events that completely or almost completely overlap each other, due to the inherent resolution limits of the technique. However, there was also no discernible difference between the 16 kHz and 100 kHz data-sets, so it appears that a 16 kHz data acquisition rate is sufficient for the maximum level of accuracy that can currently be obtained.

4.4. Event velocity statistics and scaling

Using the procedure outlined above to better discriminate between single and overlapping events, the correlation between slip event size and peak velocity during slip events can be compared to both previous experiments [5] and theoretical mean-field predictions [18,39]. The peak velocity and the event size both cover about two orders of magnitude, with the lower limit on size

determined by the thresholding procedure that was used to extract the displacement jumps (i.e. the size of the smallest event that could be distinguished from noise) and the upper limit determined by the maximum event size observed. Figure 8a displays the observed size-velocity scaling, which consists of possible power-law scaling with an exponent $n = 0.77 \pm 0.01$ ($R^2 = 0.85$).

A similar size-velocity scaling has been obtained from intermittent deformation curves of small-scale Mo crystals [5]. There the scaling appeared bimodal, with one subset of the data following a scaling law of $n = 1$ and a different subset following $n = 0.5$ (with a low number of intermediate events). A scaling exponent of $n = 0.8$ was reported for all of the data taken together, which numerically appears similar to the value found here.

Repeating the size-velocity analysis on the data presented here without using the outlined procedure of event separation gives a very similar scaling exponent ($n = 0.73 \pm 0.06$), but with a noticeably worse fit ($R^2 = 0.62$) and increased uncertainty due to increased scatter in the maximum velocity values of events between approximately 1 to 7 nm in size. Despite the increased scatter, the bimodal trend observed in Ref. [5] remains absent, and cannot be further addressed. While Ref. [5] investigated a different crystal structure (BCC), the data sampling rate was also substantially lower (25 Hz) such that any distinction of overlapping events is not feasible.

Theoretical calculations based on mean-field theory (MFT) [18,39] indicate that the expected power-law scaling for average maximum velocity versus size for dislocation avalanches near the depinning transition is $n = 0.5$. This partially matches one of the data subsets in Ref. [5], but does not at first sight match the overall trend depicted in Fig. 8a. Statistically, this conclusion is difficult to substantiate due to the limited range of data available, which becomes even smaller when considering that the lower-end of the

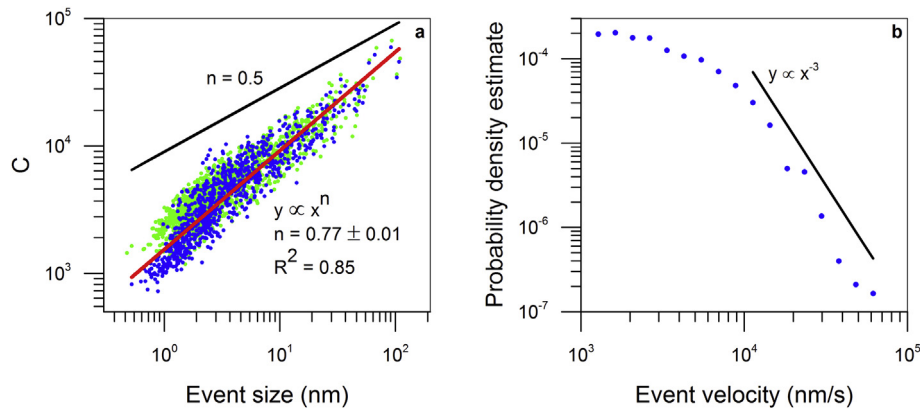


Fig. 8. a) Log-log scatter plot of size-velocity scaling obtained from Au columns (blue data), with a fit showing power-law scaling and a comparison with scaling exponent $n = 0.5$ from MFT calculations. The green data is the same raw data with different noise filtering, showing the sensitivity of the scaling to the choice of filter settings. b) Probability density estimate for peak event velocity, with line showing inverse cubic scaling for comparison (scaling from MFT and other experiments). (For interpretation of the references to colour in this figure legend, the reader is referred to the web version of this article.)

event velocity falls outside of any scaling regime, as can be more clearly seen in the plot of the probability density of the slip-velocity (given in Fig. 8b). Additionally, the measured scaling exponent appears to be sensitive to the choice of filter parameters, as shown by the green data in Fig. 8a, making a reliable determination from experimental data difficult.

As in earlier experimental work [19,20] and also as obtained from 3D-DD simulations [21], the higher-end of the slip-velocity distribution is compatible with a cubic scaling regime, whereas the slow event-velocities tend to exhibit a flat shoulder for velocities that here falls below 10^4 nm/s. An inverse cubic power-law scaling of the stress integrated mean slip-velocity distribution is predicted by MFT and thus is compatible with our data [18,40]. We also examined the duration distribution scaling for comparison with theory and models [18,36,40], but the range of durations in the cleaned data was too small for a reliable determination of a scaling exponent (less than half an order of magnitude).

Careful examination of Fig. 8a shows that the size-velocity correlation contains a clear change in behavior for values lower than ca. 6×10^3 nm/s, leaving a small data-set for higher velocities that would exhibit a lower scaling exponent than 0.78. However, the limitations in range make reliable determinations of n impossible. This restriction indicates that any further efforts to better resolve a size-velocity scaling may be experimentally inaccessible with the investigated material, because the current data-set of ca. 1400 events is unlikely to significantly increase in either slip-velocity or slip-size range. As such, even upon separation of overlapping events and therefore clarifying the origin of a bimodal slip-size vs. slip-duration distribution, at this stage the new data supports the MFT prediction [18,40] and DD results [21] by constructing the integrated velocity distribution.

4.5. Dislocation velocities versus measured slip-velocities

In light of the above results suggesting that plastic deformation is indeed occurring during the slip events and that those slip events are accurately measured, the substantial discrepancy between the observed slip event velocities and the velocities of individual dislocations will now be discussed.

The data presented here on Au crystals showed slip-velocities in the range of 1–100 $\mu\text{m/s}$, with a mean value of approximately 6 $\mu\text{m/s}$, which is remarkably similar to that shown much earlier in high-resolution slip measurements made on macroscopic single-crystals of zinc [3] and aluminum [41]. This contrasts with the observation

that individual dislocations move with a velocity on the order of m/s in Cu-(0 to 1.29 at%)Al single-crystals [42,43], tens of cm/s in neutron-irradiated Cu single-crystals [44], or tens of mm/s in Cu-(2–10%)Ni single-crystals [45], as well as the well-known result that at stresses above the critical resolved shear stress (CRSS) dislocations tend to move at very high velocity, with the maximum converging to the speed of sound in the crystal [22–24]. Given the size-effect strengthening of the micro-columns, the resolved shear stress on the slip planes is substantially above the macroscopic CRSS, and it would be expected that dislocation velocities should be near the speed of sound. Not only are the slip events much slower, but it has been shown that their velocity appears to be independent of applied stress and crystal size [19], unlike the highly stress-sensitive dislocation velocity. The origin of the stress insensitivity was discussed in Ref. [19], and one remaining question is how the low absolute velocity values seen in Fig. 4 can be understood?

One possible interpretation of this behavior is found in an experiment involving slip-line cinematography of thin, plate-shaped single-crystals [45]. Slip-lines grow both laterally and vertically on the surface of the crystal during deformation, as shown in Fig. 9a. Assuming a repeating point source of dislocation loops on the slip plane and a thin, flat crystal (as in Ref. [45]), the edge components of the loop very quickly reach the opposite face of the crystal, leaving behind a series of screw dislocations moving laterally through the crystal. While the lateral growth rate of a slip-line on the crystal surface during rapid, discrete slip events (identified with the velocity of a group of mobile screw dislocations) was 30–40 mm/s, the vertical growth rate of the same slip-line (i.e., the velocity of slip in the slip direction) was on the order of a few $\mu\text{m/s}$. This dramatic difference in velocity is due to the differing magnitudes of the distance moved laterally by a dislocation (~several mm) and the vertical slip generated by the movement of the same dislocation (1 Burgers vector, <1 nm). Such slip, as projected onto the column axis, is what is measured during micro-column compression testing. The factor determining the slip rate at any point is then the magnitude of the Burgers vector of a single dislocation divided by the rate of dislocations passing that point, which (in the limit of very high dislocation velocities) becomes limited by the repetition rate of the dislocation source.

Using the known difference in velocity between the lateral and vertical growth of the slip-step in Ref. [45], the spacing between individual dislocations in the moving group was calculated as 4–5 μm (which is consistent with other measurements of dislocation spacing in the same material using the etch-pit method).

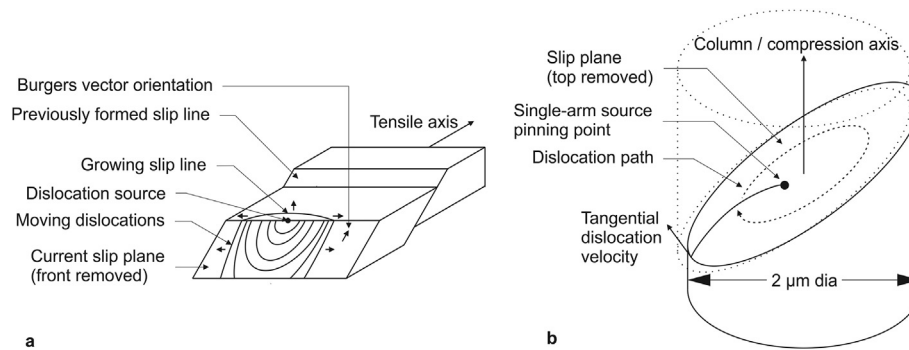


Fig. 9. a) Schematic of dislocation movement in thin plate-shaped crystals. b) Schematic of possible dislocation movement around a single-ended spiral source during slip events in micro-columns.

Given that the dislocations in the group all have similar velocities of 30–40 mm/s, this spatial separation also corresponds to a temporal separation on the order of 100 μs . In comparison, taking the mean slip-size for the gold data presented in this paper of 6.2 nm, the mean slip event duration of 1.6 ms, the Burgers vector magnitude of gold (0.2884 nm), and the projection factor of 2 from the slip plane to the compression axis, we determine that the average time interval between dislocations passing a point during a slip event should be on the order of 50 μs . One possible type of dislocation source in micro-crystals is the single-arm spiral source [46]. Given the assumption of a single-ended spiral dislocation source sweeping through the crystal along the slip plane (an elliptical cross-section at 45° to the column axis, as shown in Fig. 9b) and a column diameter of 2 μm , this would require a linear dislocation velocity (measured along the circumference of the slip plane) on the order of 150 mm/s. There could also be multiple sources active on multiple planes, in which case (given the fixed overall slip rate) the dislocation velocity on a given plane would be inversely proportional to the number of active sources. Notably, 50 μs is below the sampling interval with a data acquisition rate of 16 kHz, and even at 100 kHz observation of motion from a single dislocation would be difficult or impossible due to the small signal relative to the system noise and the low number of data points available in such a short interval. Thus, a given slip event would be expected to appear as a “continuous” movement, even though the motion of individual dislocations is fundamentally discrete. Naturally, this proposed mechanism results in a size effect, because smaller diameter would lead to a shorter circumference and thus the measured slip-velocity would be expected to increase. This was not the case in Ref. [19], but given the on average decreasing number of available sources with decreasing sample size, it is expected that the likelihood of simultaneously operating sources decreases, which therefore has to counterbalance the geometrical effect. Further research efforts will be required to properly address the detailed microstructural mechanisms that underlie a displacement jump seen in experimental stress-strain data.

5. Conclusions

In this work, slip-velocities from micro-crystals deformed in compression were measured directly during the intermittent stress-strain response. To firstly validate the experimental approach of using a nanoindentation platform to trace the temporal profile of the plastic instabilities, the indenter response is modeled, and the maximum possible forward surge velocity of the device is estimated by fracture experiments on Si microbeams. The results show that the maximum velocity is of the order of mm/s with an acceleration of 10 m/s^2 , which represents an axial velocity that is ca.

3 order of magnitude larger than the crystallographic slip-velocity in the micro-crystals. During the slip events, it is found that the force recorded by the transducer is not the force actually acting on the sample, which is 10–20% lower. This, in addition with direct electrical contact measurements during a slip event, leads to the conclusion that the indenter can trace the slipping crystal without losing mechanical contact.

The spatiotemporal slip dynamics reveal largely scattered, but low slip-velocities in the range of 1–100 $\mu\text{m/s}$. Overlapping slip events were separated out by carefully tracing the velocity profiles, which results in a strong correlation between slip-size and velocity that can be described with a power-law, which also applies to the statistical distribution of peak velocities. The measured slip-velocities are considerably slower than what one would expect for the classical correlation between stress and dislocation velocity. This difference is rationalized by differentiating between the actual speed of a dislocation segment and the speed at which a slip-step grows, leading to an approximate dislocation velocity of the order of 100 mm/s; a velocity that is well in agreement with direct etch-pit measurements of moving dislocations.

Acknowledgements

This research was carried out in part in the Frederick Seitz Materials Research Laboratory Central Research Facilities, University of Illinois. G.S. and R.M. especially thank Kathy Walsh for experimental support with the Hysitron TriboIndenter. R.M. gratefully acknowledges startup funding from the Department of Materials Science and Engineering at UIUC. R.M. is also thankful for fruitful discussions with Peter. M. Derlet, and institutional support by C.A. Volkert at his previous affiliation at the University of Goettingen. G.S. and R.M. thank Oden Warren, Douglas Stauffer, and Warren Oliver for technical discussions.

References

- [1] I.V. Shashkov, M.A. Lebyodkin, T.A. Lebedkina, Multiscale study of acoustic emission during smooth and jerky flow in an AlMg alloy, *Acta Mater.* 60 (2012) 6842–6850.
- [2] R.F. Tinder, J.P. Trzil, Millimicroplastic burst phenomena in zinc monocrystals, *Acta Metall.* 21 (1973) 975–989.
- [3] R. Becker, E. Orowan, Über sprunghafte Dehnung von Zinkkristallen, *Z. für Phys.* 79 (1932) 566–572.
- [4] J. Weiss, D. Marsan, Three-dimensional mapping of dislocation avalanches: clustering and space/time coupling, *Science* 299 (2003) 89–92.
- [5] M. Zaiser, J. Schwerdtfeger, A.S. Schneider, C.P. Frick, B.G. Clark, P.A. Gruber, E. Arzt, Strain bursts in plastically deforming molybdenum micro- and nanopillars, *Philos. Mag.* 88 (2008) 3861–3874.
- [6] D.M. Dimiduk, C. Woodward, R. Lesar, M.D. Uchic, Scale-free intermittent flow in crystal plasticity, *Science* 312 (2006) 1188–1190.

- [7] R. Maaß, C.A. Volkert, P.M. Derlet, Crystal size effect in two dimensions – influence of size and shape, *Scr. Mater.* 102 (2015) 27–30.
- [8] S. Brinckmann, J.Y. Kim, J.R. Greer, Fundamental differences in mechanical behavior between two types of crystals at the nanoscale, *Phys. Rev. Lett.* 100 (2008) 155502.
- [9] N. Friedman, A.T. Jennings, G. Tsekenis, J.Y. Kim, M. Tao, J.T. Uhl, J.R. Greer, K.A. Dahmen, Statistics of dislocation slip avalanches in nanosized single crystals show tuned critical behavior predicted by a simple mean field model, *Phys. Rev. Lett.* 109 (2012) 095507.
- [10] D.M. Dimiduk, E.M. Nadgorny, C. Woodward, M.D. Uchic, P.A. Shade, An experimental investigation of intermittent flow and strain burst scaling behavior in LiF crystals during microcompression testing, *Philos. Mag.* 90 (2010) 3621–3649.
- [11] R. Maass, M. Wraith, J.T. Uhl, J.R. Greer, K.A. Dahmen, Slip statistics of dislocation avalanches under different loading modes, *Phys. Rev. E Stat. Nonlin Soft Matter Phys.* 91 (2015) 042403.
- [12] J. Alcalá, J. Ocenasek, K. Nowag, D. Esque-de los Ojos, R. Ghisleni, J. Michler, Strain hardening and dislocation avalanches in micrometer-sized dimensions, *Acta Mater.* 91 (2015) 255–266.
- [13] P.D. Ispanovity, L. Laurson, M. Zaiser, I. Groma, S. Zapperi, M.J. Alava, Avalanches in 2D dislocation systems: plastic yielding is not depinning, *Phys. Rev. Lett.* 112 (2014) 235501.
- [14] S. Papanikolaou, D.M. Dimiduk, W. Choi, J.P. Sethna, M.D. Uchic, C.F. Woodward, S. Zapperi, Quasi-periodic events in crystal plasticity and the self-organized avalanche oscillator, *Nature* 490 (2012) 517–521.
- [15] M. Zaiser, Scale invariance in plastic flow of crystalline solids, *Adv. Phys.* 55 (2006) 185–245.
- [16] F.F. Csikor, C. Motz, D. Weygand, M. Zaiser, S. Zapperi, Dislocation avalanches, strain bursts, and the problem of plastic forming at the micrometer scale, *Science* 318 (2007) 251–254.
- [17] P.M. Derlet, R. Maass, Micro-plasticity and intermittent dislocation activity in a simplified micro-structural model, *Model. Simul. Mater. Sci. Eng.* 21 (2013) 035007.
- [18] M. LeBlanc, L. Angheluta, K. Dahmen, N. Goldenfeld, Universal fluctuations and extreme statistics of avalanches near the depinning transition, *Phys. Rev. E Stat. Nonlin Soft Matter Phys.* 87 (2013) 022126.
- [19] R. Maass, P.M. Derlet, J.R. Greer, Independence of slip velocities on applied stress in small crystals, *Small* 11 (2015) 341–351.
- [20] R. Maass, P.M. Derlet, J.R. Greer, Small-scale plasticity: insights into dislocation avalanche velocities, *Scr. Mater.* 69 (2013) 586–589.
- [21] P.D. Ispanovity, I. Groma, G. Gyorgyi, F.F. Csikor, D. Weygand, Submicron plasticity: yield stress, dislocation avalanches, and velocity distribution, *Phys. Rev. Lett.* 105 (2010) 085503.
- [22] H. Neuhäuser, Slip-line formation and collective dislocation motion, in: F.R.N. Nabarro (Ed.), *Dislocations in Solids*, vol. 6, North-Holland Publishing Company, Amsterdam, 1983, pp. 319–440.
- [23] W.G. Johnston, J.J. Gilman, Dislocation velocities, dislocation densities, and plastic flow in lithium fluoride crystals, *J. Appl. Phys.* 30 (1959) 129.
- [24] K.M. Jassby, T. Vreeland, An experimental study of the mobility of edge dislocations in pure copper single crystals, *Philos. Mag.* 21 (1970) 1147–1168.
- [25] V.A. Al'shitz, V.L. Indenbom, Dynamic dragging of dislocations, *Sov. Phys. Uspekhi* 18 (1975) 1–20.
- [26] F.R.N. Nabarro, H. Conrad, Low-speed dislocations, in: A.R. Rosenfield, G.T. Hahn, A.L. Bement, R.I. Jaffee (Eds.), *Dislocation Dynamics - Materials Science and Engineering Series*, 1968, pp. 475–484. New York.
- [27] J. Hay, P. Agee, E. Herbert, Continuous stiffness measurement during instrumented indentation testing, *Exp. Tech.* 34 (2010) 86–94.
- [28] S. Ruffell, J.E. Bradby, J.S. Williams, O.L. Warren, An in situ electrical measurement technique via a conducting diamond tip for nanoindentation in silicon, *J. Mater. Res.* 22 (2007) 578–586.
- [29] D.D. Stauffer, R.C. Major, D. Vodnick, J.H. Thomas III, J. Parker, M. Manno, C. Leighton, W.W. Gerberich, Plastic response of the native oxide on Cr and Al thin films from in situ conductive nanoindentation, *J. Mater. Res.* 27 (2012) 685–693.
- [30] J.K. Heyer, S. Brinckmann, J. Pfetzinger-Micklich, G. Eggeler, Microshear deformation of gold single crystals, *Acta Mater.* 62 (2014) 225–238.
- [31] R. Maaß, J.F. Löffler, Shear-band dynamics in metallic glasses, *Adv. Funct. Mater.* 25 (2015) 2353–2368.
- [32] R. Maaß, D. Klaumünzer, J.F. Löffler, Propagation dynamics of individual shear bands during inhomogeneous flow in a Zr-based bulk metallic glass, *Acta Mater.* 59 (2011) 3205–3213.
- [33] Y.Q. Cheng, Z. Han, Y. Li, E. Ma, Cold versus hot shear banding in bulk metallic glass, *Phys. Rev. B* 80 (2009).
- [34] C.Q. Chen, Y.T. Pei, J.T.M. De Hosson, Effects of size on the mechanical response of metallic glasses investigated through in situ TEM bending and compression experiments, *Acta Mater.* 58 (2010) 189–200.
- [35] X. Zhang, B. Pan, F. Shang, Scale-free behavior of displacement bursts: lower limit and scaling exponent, *EPL Europhys. Lett.* 100 (2012) 16005.
- [36] X. Zhang, F. Shang, Y. Yu, Y. Yan, S. Yan, A stochastic model for the temporal aspects of flow intermittency in micropillar compression, *Int. J. Solids Struct.* 51 (2014) 4519–4530.
- [37] J.R. Greer, W.D. Nix, Size dependence of mechanical properties of gold at the sub-micron scale, *Appl. Phys. A Mater.* 80 (2005) 1625–1629.
- [38] H. Zhang, B.E. Schuster, Q. Wei, K.T. Ramesh, The design of accurate micro-compression experiments, *Scr. Mater.* 54 (2006) 181–186.
- [39] J. Antonaglia, W.J. Wright, X. Gu, R.R. Byer, T.C. Hufnagel, M. LeBlanc, J.T. Uhl, K.A. Dahmen, Bulk metallic glasses deform via slip avalanches, *Phys. Rev. Lett.* 112 (2014) 155501.
- [40] A. Dobrinevski, P. Le Doussal, K.J. Wiese, Avalanche shape and exponents beyond mean-field theory, *EPL Europhys. Lett.* 108 (2014) 66002.
- [41] R. Becker, P. Haasen, Kinematographie von gleitlinien auf Al-Einkristallen, *Acta Metall.* 1 (1953) 325–335.
- [42] M. Kleintges, R. Labusch, H.G. Brion, P. Haasen, Measurement of dislocation velocities in Cu-Al single crystals—I, *Acta Metall.* 25 (1977) 1247–1255.
- [43] H. Ney, R. Labusch, P. Haasen, Measurement of dislocation velocities in Cu-Al single crystals—II, *Acta Metall.* 25 (1977) 1257–1269.
- [44] H.H. Potthoff, Velocities of dislocation groups in very thin neutron-irradiated copper single crystals measured by slip line cinematography, *Phys. Status Solidi (a)* 77 (1983) 215–224.
- [45] O.B. Arkan, H. Neuhäuser, Dislocation velocities in Cu-Ni alloys determined by the stress pulse-etch pit technique and by slip line cinematography, *Phys. Status Solidi (a)* 99 (1987) 385–397.
- [46] S.I. Rao, D.M. Dimiduk, M. Tang, M.D. Uchic, T.A. Parthasarathy, C. Woodward, Estimating the strength of single-ended dislocation sources in micron-sized single crystals, *Philos. Mag.* 87 (2007) 4777–4794.